AIAA JOURNAL
Vol. 47, No. 4, April 2009

Density Measurements in a Supersonic Microjet Using Miniature Rainbow Schlieren Deflectometry

Pankaj S. Kolhe* and Ajay K. Agrawal†
University of Alabama, Tuscaloosa, Alabama 35487

DOI: 10.2514/1.37332

Understanding of the structure of complex supersonic flows requires high-resolution, nonintrusive measurements across the whole field. The measurement requirements are even more challenging when dealing with small-scale systems. In this study, we apply the miniature rainbow schlieren deflectometry system to measure the density field in underexpanded microjets from an orifice injector of 500 μm diameter. The injector is used to replicate the practical scenario of accidental leakage from a compressed gas storage facility. Experiments were conducted for a range of supply pressures P_s, although the majority of the results are presented for $P_s = 860$ kPa. Experimental schlieren images were analyzed to determine the density contours in an axisymmetric domain with a field of view of 1.5 mm radius and 7.5 mm length, at a spatial resolution of 25 μm. Pressure, temperature, and Mach number profiles (normalized by the values at the orifice) were also obtained along the jet centerline. Results show features similar to those observed in underexpanded macrojet from a sonic nozzle; multiple shock-cell structures with expansion and compression fans, freejet boundary, incident, normal, and reflected shock waves, subsonic slip strip, and outer shear layer. The miniature rainbow schlieren deflectometry technique is shown to provide high-quality quantitative data to explain the structural details of underexpanded microjets.

I. Introduction

THE study of supersonic jets is an important subject in gas dynamics because of their numerous engineering applications. Detailed understanding of the supersonic jet dynamics requires the knowledge of vector (viz. velocity) and scalar (viz. density, pressure, and temperature) quantities throughout the flow field. Such information is often obtained from numerical studies, taking into account various phenomena of shock wave interactions. In the past, several studies have been conducted to compute the structure of supersonic jet flows [1,2]. However, validation requires detailed experimental measurements of the relevant flow properties. Typically, measurements in supersonic flows are obtained by intrusive static or total pressure probes and hot-wire anemometer. However, such probes introduce significant measurement errors, especially if the flow field contains multiple shock wave regions, for example, in underexpanded jets. Moreover, intrusive probes have poor spatial and temporal resolutions, and measurements are obtained point by point. Thus, nonintrusive techniques for whole field measurements are necessary to infer the structural details of complex supersonic jets.

Several line-of-sight and local measurement techniques have been used to study supersonic jets. Dillman et al. [3] employed Mach–Zehnder interferometry to measure the density field in cylindrical, turbulent supersonic jets. Sequential interferograms obtained across the field of view were time-averaged to determine the mean density distributions. Faris and Byer [4] used a laser beam deflection technique to obtain point measurements of density in a supersonic nitrogen jet. Lee et al. [5] and Naik et al. [6] used a planar nitric oxide laser induced fluorescence technique to measure the scalar properties such as the pressure and temperature in underexpanded jets. However, the jet diameters used in these studies were of the order of a few millimeters, and the seeding of nitric oxide with air was required. Woodmansee et al. [7] demonstrated a coherent anti-Stokes Raman scattering (CARS) technique to measure pressure and temperature along the centerline of an underexpanded jet. Panda and Seasholtz [8,9] used a filtered Rayleigh scattering technique to measure vector–scalar fields in supersonic free jets and to study shock–vortex interactions in underexpanded jets. In both CARS and Rayleigh scattering techniques, point measurements were obtained by traversing the probe volume within the flow field of interest. None of the preceding techniques is in wide-spread use for measurements in supersonic flows, in part, because of the difficulties in configuring the optical system, specific experimental and/or seeding requirements, limited spatial and/or temporal resolutions, and the need to traverse the probe volume across the whole field of view. These problems are accentuated in miniature flow systems that are the focus of the present study.

In recent years, the scientific community has seen remarkable progress in the area of microscale devices with applications ranging from propulsion, power generation, and biochemical devices. For example, in the aerospace industry, micron-size nozzles measuring approximately 35 μm are being designed for use in microthrusters [10,11]. A supersonic jet constitutes a concentrated source of cooling fluid for heat removal because of inherently high flow velocities and a smaller jet spreading angle. Supersonic microjets can also be used as actuators to control the ground effects created by macroscale impinging supersonic jets, generally observed in short take off and vertical landing aircraft [12]. The small length scales make the task of acquiring quantitative, nonintrusive measurements in supersonic microjets extremely challenging.

Although several techniques to measure the velocity field in miniature systems have been developed [13–17], similar diagnostics of scalar fields (e.g., temperature, pressure, density, and species concentration) have received little attention. Scroggs and Settles [18] studied the scalar flow structure in converging–diverging nozzles of diameter ranging from 600 to 1200 μm. Results show a postponed transition to turbulence with the reduction in the length scale. Phalnikar et al. [19,20] used a knife-edge schlieren system to visualize the shock-cell structures in free and impinging supersonic microjets of an inside diameter varying from 100 to 400 μm. The schlieren images clearly showed the characteristic shock-cell structure typically observed in larger supersonic jets. In addition to providing detailed qualitative data, the microschlieren images were used to obtain quantitative information such as shock-cell spacing

Presented as Paper 238 at the Aerospace Science Meeting, Reno, NV, 4–10 January 2008; received 27 February 2008; revision received 10 October 2008; accepted for publication 11 October 2008.

*Ph.D. Student, Mechanical Engineering Department; pskolhe@gmail.com. Student Member AIAA.

†Barfield Endowed Chair Professor, Mechanical Engineering Department; aagrawal@eng.ua.edu (Corresponding Author). Associate Fellow AIAA.

and supersonic core length. In these studies [18–20], a knife-edge schlieren system was used, and miniature probes were traversed across the flow field to measure pressure and/or Mach number. As pointed out by Panda and Seasholtz [9], an intrusive probe can alter the upstream reflection pattern of expansion and compression fans in an underexpanded jet, which can result in significant measurement errors. Errors associated with these intrusive probe effects can corrupt the measurements in supersonic microjets.

Recently, we presented a miniature rainbow schlieren deflectometry technique for quantitative measurements in microjets and flames [21]. The optical layout of the mRSD system is similar to that of macroscale systems [22–25], although the field of view of the former is smaller by an order of magnitude. Satti et al. [21] demonstrated the capability of the mRSD system by measuring concentration profiles in a helium microjet (diameter $d = 650$ μm) and temperature and species concentration profiles in a hydrogen jet diffusion flame from a microinjector of 50 μm diameter. The mRSD apparatus requires no laser source, the optical alignment is simple, and it is tolerant to minor mechanical imperfections and/or vibrations. In this study, we were motivated by the challenge to apply the mRSD apparatus for quantitative scalar measurements (density, pressure, and temperature) in supersonic microjets that were visualized only qualitatively by Satti et al. [21]. An underexpanded microjet exhibiting complex flow field with expansion and compression waves, and incident, reflected and normal shock waves interacting with each other was chosen as the test case. Air supplied from a compressed storage tank is chosen as the working fluid for the experiments. Rainbow schlieren images acquired at spatial resolution of 25 μm were analyzed to obtain density profiles across the whole field of view. Measurements were also used to obtain normalized pressure, temperature, and Mach number profiles along the jet centerline. Experimental and analytical details along with results and discussions are provided in the following.

II. Experimental Procedure

The optical configuration of the mRSD apparatus requires careful evaluation of each optical component and various optical issues, as discussed in detail by Satti et al. [21]. In this section, we provide a brief outline of the optical hardware followed by descriptions of the test medium and analysis procedures. The rail-mounted mRSD apparatus shown schematically in Fig. 1 consists of optical and image acquisition systems. The optical system includes broadband light from a 150 W halogen light source, transmitted by a 1000 μm

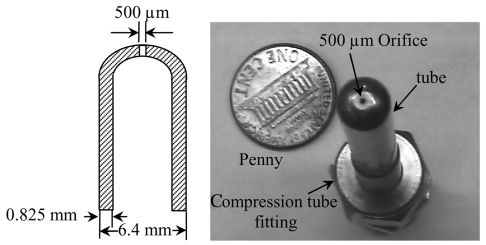

Fig. 2 Orifice injector details a) orifice tube cross section b) photograph of the injector.

fiber optic cable with its terminating end centered on a 5 μm wide, 3 mm high source aperture. The source aperture is placed at the focal point of an achromatic lens of 20 mm diameter and 80 mm focal length to obtain collimated light rays. Light rays deflected by the test medium are decollimated by a 20 mm diameter lens of 250 mm focal length, rendering the source image magnification factor of 3.125. The source aperture image (width $5 \times 3.125 = 15.6$ μm) displaced by the test medium is formed at the focal point of the decollimating lens, wherein a rainbow filter is placed. The rainbow filter is a continuous-grade color filter printed on a 35-mm slide film at a spatial resolution of 8.5 μm (i.e., the width of each unique color strip is 8.5 μm). The filtered rainbow schlieren image is acquired by the image acquisition system comprising a charge-coupled-device array fitted with a camera lens and extension tubes. The charge-coupled device imager is a Redlake HG_TX CR2000 camera operated at an image acquisition rate of 60 frames/s and an exposure time of 7.0 ms. Each image acquired at 512×384 pixel resolution is digitized and downloaded as 24 bit color TIFF file. Irrespective of the demosaicing pattern used by the camera, hue is computed at each pixel location. Based on the physical and imaged dimensions of the injector tube, the spatial resolution in the schlieren image is 25 μm. Based on the magnification employed and the camera lens effective modulation transfer function, the estimated diffraction limited spatial resolution is 6 μm. The Rayleigh-criterion-based diffraction limited spatial resolution for the decollimating lens is estimated to vary from 5 to 8.8 μm. Thus, the diffraction effects are negligible for the reported spatial resolution of 25 μm.

The test medium consists of an underexpanded air jet discharged into the ambient from a vertically oriented orifice injector of a diameter $d = 500$ μm, as shown schematically in Fig. 2a. Figure 2b shows a close-up view of the orifice injector attached to a

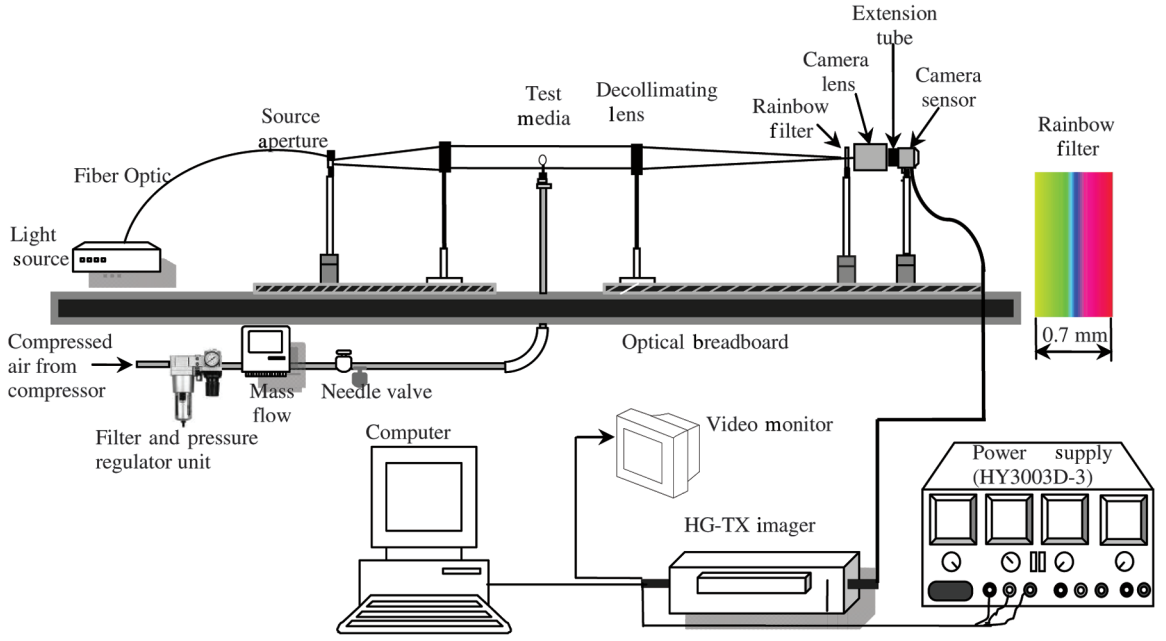

Fig. 1 Experimental set up with the schlieren apparatus and rainbow filter.

compression tube fitting. The orifice injector used in this study replicates the practical scenario of accidental leakage from compressed gas storage facilities, and its geometry differs from the contoured sonic nozzle used in previous studies. The airflow supply line consists of a compressed storage tank, an air filter/pressure regulator assembly, a mass flow meter, and a needle valve to regulate and measure the mass flow rate. Based on flow visualization in different schlieren modes and at various times, the supersonic jets were found to produce a steady and axisymmetric flow field for the present operating conditions.

III. Schlieren Analysis

The mRSD technique measures the deflection of light rays passing through a medium with refractive index (or density) gradients. In general, the test medium density varies both in transverse and axial directions, and, hence, a light ray will deflect in both of these directions. Upon decollimation, the deflected ray produces displacement (transverse and axial) at the filter plane. The color strips on the rainbow filter, shown in Fig. 3, transmit a unique color depending upon the location of the light ray on the filter plane. Light rays passing through different parts of the test medium deflect and displace differently, and, hence, they assume different colors downstream of the filer plane to produce the so-called rainbow schlieren image. The rainbow filter serves as a fine ruler to accurately measure the ray displacement at the filter plane, in terms of the transmitted color in the rainbow schlieren image quantified by hue according to the HSI (hue saturation intensity) color model [22]. Here, HSI parameters are obtained by transformation from the (red green blue) color model. The HSI model has the advantage of specifying color by a single parameter, hue, unlike the three attributes required in the RGB color model [for additional details refer Greenberg et al. [22]]. The rainbow filter is sensitive only to the transverse displacements if color strips and source aperture are aligned with the axial direction, and vice versa. In this study, the aperture and rainbow filter were oriented to detect the density gradients only in the transverse direction. For an axisymmetric medium, the transverse ray deflection angle is given by

$$\varepsilon(y) = 2y \cdot \int_y^\infty \frac{\partial \delta}{\partial r} \frac{\mathrm{d}r}{\sqrt{r^2 - y^2}} \tag{1}$$

Here, δ is the normalized refractive index difference [$\delta = (\eta - \eta_0)/\eta_0$], η is the refractive index of the medium, η_0 is the refractive index of surroundings, r is the radial coordinate, and y is the offset distance from the jet axis. The transverse displacement of a ray at the filter plane is

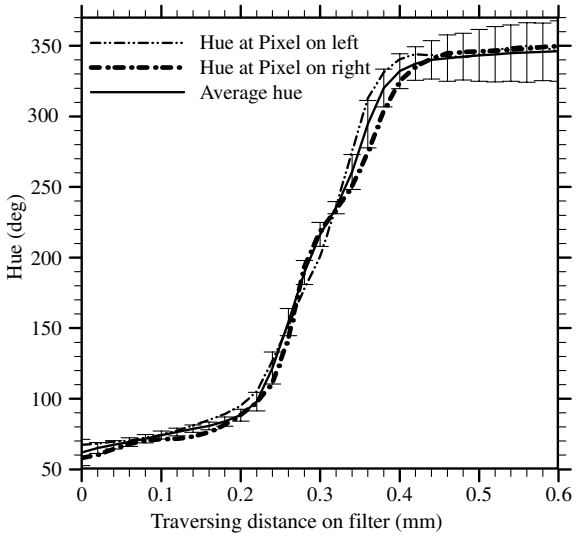

Fig. 4 Filter calibration curves based on average image hue and hue at a pixel.

$$d(y) = \varepsilon(y).f \tag{2}$$

where f is the focal length of the decollimating lens.

The schlieren analysis requires the rainbow filter calibration curve relating transmitted hue to the transverse position on the filter plane. The filter calibration curve is generated by acquiring the background rainbow schlieren images (images obtained without the test medium) at different filter positions. Figure 3 shows background schlieren images acquired at selected filter locations. Typically, the hue in the background image of the mRSD system is nearly uniform. Thus, an average hue can be computed from the background schlieren image for each filter position to generate the filter calibration curve shown by the solid line in Fig. 4. However, in the mRSD system, the background hue can vary significantly as shown by the error bars of the standard deviation of hue in Fig. 4. Hue variations in the background schlieren image are caused by the inaccuracies in printing a small-width (less than 1 mm) filter, minor optical misalignments, and chromatic aberrations. Hue measurement uncertainties will inevitably propagate into uncertainties in measurements of density and related scalar properties. In this study, we obtain filter calibration curves at each pixel location to essentially eliminate the hue measurement uncertainties. Figure 4 shows the filter calibration curves at two different pixel locations. Note that the

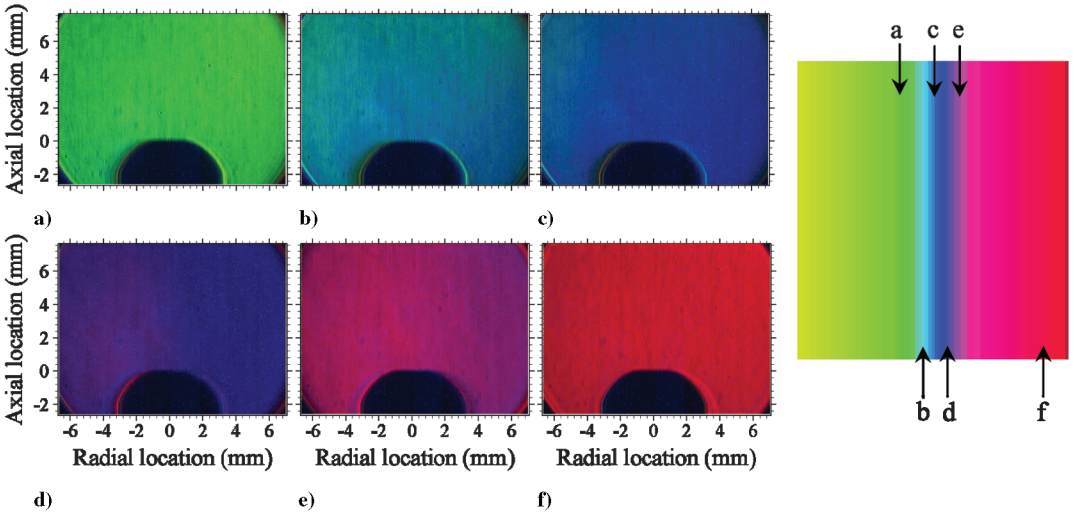

Fig. 3 Background schlieren images at different traversing distances across the filter.

pixel-based filter calibration curves deviate slightly from the average image hue-based filter calibration curve.

The schlieren images without and with the test medium are acquired without disturbing the optical system or the experimental setup. This practice ensures that a given pixel in the schlieren image without or with the test medium maps the same physical location. In the analysis procedure for each pixel location in the schlieren image, the measured hue H is converted to a transverse position on the filter plane X, according to the filter calibration curve for a particular pixel location, that is

$$X(H) = X_i + \frac{X_{i+1} - X_i}{H_{i+1} - H_i} \cdot (H_{i+1} - H) \tag{3}$$

where $(X_i, H_i)$and (X_{i+1}, H_{i+1}) are the filter calibration coordinates closest to the measured hue H. In this study, the filter calibration curves were generated by traversing the filter at intervals of 20 μm to minimize errors associated with the linear interpolation in Eq. (3).

Next, the transverse deflection angle of a light ray is found by rearranging Eq. (2) as

$$\varepsilon(y) = \frac{d(y)}{f} = \frac{X(H) - X(H_b)}{f} \tag{4}$$

where $X(H_b)$ is the transverse filter position pertaining to the background hue H_b (i.e., hue value at the pixel in a schlieren image without the test medium). Pixel-to-pixel filter calibration ensures that the demosaicing pattern used by the camera to estimate hue at each pixel location would not introduce errors in deflection-angle estimation. Note that the deflection angles in the background image (i.e., schlieren image without the test medium) are zero indicating that no density gradients are present in the absence of the test medium.

Next, the normalized refractive index difference is found from the Abel inversion of Eq. (1) given as

$$\delta(r) = \frac{-1}{\pi} \int_r^\infty \varepsilon(y) \cdot \frac{\mathrm{d}y}{\sqrt{y^2 - r^2}} \tag{5}$$

The integral in Eq. (5) is solved numerically as

$$\delta(r_i) = \sum_{j=1}^{n+1} D_{ij} \varepsilon_j \tag{6}$$

where the geometric coefficient D_{ij} is given by Agrawal et al. [26]. The normalized refractive index difference is related to density by the Gladstone–Dale relationship given as

$$\rho = \frac{\delta}{\kappa} \tag{7}$$

where k is the Gladstone–Dale constant. In an isentropic flow, the density is related to pressure and temperature as

$$\frac{P}{P_e} = \left(\frac{\rho}{\rho_e}\right)^{\gamma} \tag{8a}$$

$$\frac{T}{T_e} = \left(\frac{\rho}{\rho_e}\right)^{(\gamma-1)} \tag{8b}$$

where γ is the ratio of specific heats. In a supersonic flow, the isentropic relations provide good representation in the expansion and compression wave regions. Isentropic relations could also be used across the weak shock regions. For example, for density ratio of less than 2.0 across a normal shock, the pressure ratios computed from isentropic relation and Rankine–Hugoniot relations are within 4% of each other [27]. Thus, isentropic relations are used in the present study to determine normalized pressure and temperature along the jet centerline P/P_e and T/T_e, whereby the orifice exit values P_e and T_e are used for normalization. Finally, the normalized Mach number M/M_e, where M_e is the Mach number at the orifice exit, is obtained from the continuity equation expressed as

$$\frac{M}{M_e} = \left(\frac{\rho_e}{\rho}\right)^{\frac{\gamma+1}{2}} \tag{9}$$

IV. Uncertainty Analysis

Measured quantities (independent variables) in diagnostics systems are used to obtain derived quantities (dependent variables) based on the relevant data reduction equations [28]. The schlieren analysis involves several data reduction steps, each one affecting the propagation of the measurement uncertainties. The elemental error sources in the experimentation and analysis procedure identified are listed as follows: 1) bias error in a screw gauge used to traverse the filter for calibration ($B_X = 1$ μm), 2) precision error in traversing the filter ($P_X = B_X = 50\%$ of least count of screw gauge $= 5$ μm), 3) error in the focal length of the decollimating lens ($U_f = 5$ mm), 4) error in the Gladstone–Dale constant ($U_k = 1\%$ of κ or 2.274×10^{-6}), and 5) error in the estimate of the specific heat ratio ($U_\gamma = 1\%$ of γ or 0.014).

The first three error sources are involved in estimating the deflection angle and the last two error sources stem from the assumptions in the analysis procedure to extract the scalar fields. The bias and precision errors in the filter calibration process takes into account the hue position uncertainty. The focal length uncertainty of 5 mm is a rather conservative estimate and it accounts for the minor chromatic aberrations in the lens and uncertainties in the optical alignment upstream of the decollimating lens. The hue measurement uncertainty in neglected because the filter is calibrated at the pixel location. The uncertainty in Gladstone–Dale constant relates to the minor variation with the wavelength of light. Besides the error in the specific heat ratio, the uncertainties in scalar variables derived from density include errors introduced by the isentropic relations across the normal shock.

The uncertainty in calibrating the filter includes the bias and precision errors expressed by

$$U_{X_i} = U_{X_{i+1}} = \sqrt{B_X^2 + P_X^2} \tag{10}$$

The uncertainty in the transverse location on the filter plane corresponding to the hue measured in the rainbow schlieren image [refer Eq. (3)] is given by

$$U_{X(H)} = \sqrt{\left(\left(\frac{\partial X(H)}{\partial X_i}\right)^2 \cdot U_{X_i}^2 + \left(\frac{\partial X(H)}{\partial X_{i+1}}\right)^2 \cdot U_{X_{i+1}}^2 + 2\left(\frac{\partial X(H)}{\partial X_i}\right)\left(\frac{\partial X(H)}{\partial X_{i+1}}\right) B_{X_i} . B_{X_{i+1}}\right)} \tag{11}$$

where $\frac{\partial X(H)}{\partial X_i} = (1 - \frac{H_{i+1}-H}{H_{i+1}-H_i})$, $\frac{\partial X(H)}{\partial X_{i+1}} = (\frac{H_{i+1}-H}{H_{i+1}-H_i})$, and $B_{X_i} = B_{X_{i+1}} = B_X$.

Following Eq. (4), the propagated uncertainty in deflection angle is given by

$$U_\varepsilon = \sqrt{\left(\frac{\partial \varepsilon}{\partial X(H)}\right)^2 \cdot U_{X(H)}^2 + \left(\frac{\partial \varepsilon}{\partial X(H_b)}\right)^2 \cdot U_{X(H_b)}^2 + \left(\frac{\partial \varepsilon}{\partial f}\right)^2 \cdot U_f^2} \tag{12}$$

where $\frac{\partial \varepsilon}{\partial X(H)} = (\frac{1}{f})$, $\frac{\partial \varepsilon}{\partial X(H_b)} = (\frac{-1}{f})$, and $\frac{\partial \varepsilon}{\partial f} = (\frac{-\varepsilon}{f})$.

From the data reduction Eq. (6), the uncertainty in the refractive index difference can be written as follows:

$$U_{\delta i} = \sqrt{\sum_{j=i}^{N} \left(\left(\frac{\partial \delta_i}{\partial \varepsilon_j}\right)^2 \cdot U_{\varepsilon_j}^2\right)} \tag{13}$$

where $\frac{\partial \delta_i}{\partial \varepsilon_j} = D_{ij}$.

Following the data reduction Eq. (7) for density, the propagated uncertainty in density is given by

$$U_\rho = \sqrt{\left(\frac{\partial \rho}{\partial \delta}\right)^2 \cdot U_\delta^2 + \left(\frac{\partial \rho}{\partial \kappa}\right)^2 \cdot U_\kappa^2} \tag{14}$$

where $\frac{\partial \rho}{\partial \delta} = (\frac{1}{\kappa})$ and $\frac{\partial \rho}{\partial \kappa} = \frac{-\rho}{\kappa}$.

The uncertainty propagation in normalized pressure, temperature, and Mach number variation is estimated in a similar manner. The partial derivatives in the preceding equations are solved numerically using the finite-difference approximation. Based on the elemental errors and expressions for the error magnification factors, the uncertainty in the hue position has the highest and the uncertainty in the focal length of the decollimating lens has the least effect on the propagated uncertainty in density. Uncertainties in scalar properties derived from the density include errors associated with the difference between isentropic and Rankine–Hugoniot relations, which accumulate with the downstream distance as the flow passes through more shocks. Table 1 lists the maximum uncertainties in the dependent variables based on specified estimates of uncertainties in the elemental error sources.

V. Results and Discussion

In this section, qualitative aspects of the underexpanded microjet flow are discussed first followed by the quantitative details. Detailed results are presented for air-supply pressure of 860 kPa, although experiments were conducted for supply pressure ranging from 308 to 860 kPa.

Figure 5a shows the color schlieren image of the underexpanded microjet obtained using a symmetric filter. The scale around the image is normalized by the orifice diameter, and, hence, the physical dimensions of the radial and axial boundaries are 1.5 mm and 7.3 mm, respectively. Interestingly, the underexpanded microjet exhibits the key features of its macroscale counterpart, an observation also made by Phalnikar et al. [19,20]. Figure 5a shows the typical features of shock-cell structures appearing repeatedly in the flow field. These features, illustrated in Fig. 6, include a free supersonic jet boundary, expansion and compression fans, incident, normal, and reflected shocks, a subsonic slip strip, and an outer shear layer. Figure 5a shows a normal shock at $z/d = 1.6$, which weakens or is replaced by intersecting incident shocks in subsequent shock-cell structures. Figure 5a depicts cyclic structures in the shear layer outside the freejet boundary, which, to the best of our knowledge, have not been reported in the past literature on underexpanded microjets.

Table 1 Maximum uncertainty in the dependent variables

Dependent variable	Maximum percentage uncertainty
Density	0.92%
Pressure ratio	12.3%
Temperature ratio	7.0%
Mach number ratio	2.6%

The schlieren image in Fig. 5a was inadequate for quantitative analysis, although it offered excellent flow visualization. In the test medium of the present study, a ray can undergo either positive or negative angular deflection, which can only be resolved by an asymmetric filter shown in Fig. 3, unlike the symmetric filter used to acquire the image in Fig. 5a. Further, for quantitative analysis, the high slope region of the filter calibration curve must be used, which limits the working range of hue from about 125 to 300 deg (see Fig. 4). These constraints were used to acquire the quantitative rainbow schlieren image reproduced in Fig. 5b. Figure 5b depicts repeating shock-cell structures in the flow field, although the visual appearance of the quantitative image is inferior to the schlieren image in Fig. 5a.

In schlieren analysis, the transverse deflection angle is computed from Eq. (4) and the filter calibration curve. Figure 5c shows the contour plot of the transverse deflection angle (in radians) across the field of view. As noted previously, both negative and positive transverse deflection angles ranging from −0.0001 to 0.00008 rad are inferred from the quantitative schlieren image of Fig. 5b. The contour plot in Fig. 5c illustrates the shock-cell structures, and it also depicts noticeable changes in the flow structure between the consecutive cycles. The region with finite angular deflection varies from about $r/d = 2.0$ at the orifice exit ($z/d = 0.0$) to about $r/d = 2.4$ at $z/d = 15.0$.

Data in Fig. 5c were used with Eqs. (6) and (7) to obtain the density contour plot shown in Fig. 5d. Results show large density gradients in the radial direction, indicating highly nonuniform flow at the orifice exit. The jet flow at the exit ($z/d = 0.0$) extends up to $r/d = 2.0$ or well beyond the supersonic freejet boundary located around $r/d = 0.7$ (see Fig. 5a). In the axial direction, the shock-cell structures result in a cyclic pattern of low and high densities. For example, in the first shock-cell, a normal shock is located at $z/d = 1.6$, where the density increases rapidly. In general, the peak density decreases in the shock-cell structures located downstream. The density varies from a minimum of 1.2 kg/m^3 to a maximum of 2.4 kg/m^3, or almost by a factor of 2 within the field of view. These results agree with Rayleigh scattering density measurements in macrojets by Panda and Seasholtz [10] and with schlieren visualizations and pitot-probe measurements in microjets by Phalnikar et al. [19,20]. Results also demonstrate that the capability of the rainbow schlieren technique to resolve small-scale structures in this complex supersonic flow field is impressive, especially considering the simplicity of the experimental approach.

Next, axial and radial profiles are presented at various locations to gain understanding of the complex physical processes involved in the formation of the shock-cell structures in the underexpanded microjet. Figure 7 shows the density and normalized pressure, temperature, and Mach number profiles along the jet centerline. In Fig. 7, the measurement uncertainties are identified by error bars at every third data point. The normal-shock location and/or incident shock intersection point at the jet center, inferred from the schlieren image in Fig. 5a, is also marked in Fig. 7 for the first few shock-cell structures. In Fig. 7a, one observes density increasing from a low of 1.2 kg/m^3 at $z/d = 1.0$ to the high of 2.4 kg/m^3 at $z/d = 2.2$ or across the normal shock located at $z/d = 1.6$. This thick region of density increase suggests that in addition to the compression across the thin normal shock (at $z/d = 1.6$), the flow also compresses in the upstream supersonic region ($z/d = 1.0$ to 1.6) and the downstream subsonic region ($z/d = 1.6$ to 2.2). A similar trend is observed for the second shock-cell structure, although the normal shock, located at $z/d = 3.9$, is rather weak. The density varies in a cyclic manner with both the mean and amplitude decreasing in the streamwise direction. Interestingly, these results are consistent with the density measurements of Panda and Seasholtz [9] obtained for a sonic nozzle of 25.4 mm exit diameter (as apposed to the orifice of 0.5 mm exit diameter in the present study). These trends of the density profile are replicated by the normalized pressure, temperature, and Mach number profiles presented in Figs. 7b–7d.

An interesting observation is the increase in density (or pressure and temperature) near the orifice exit (i.e., between $z/d = 0.0$ to 0.5). Because the exit Mach number at the orifice center cannot exceed

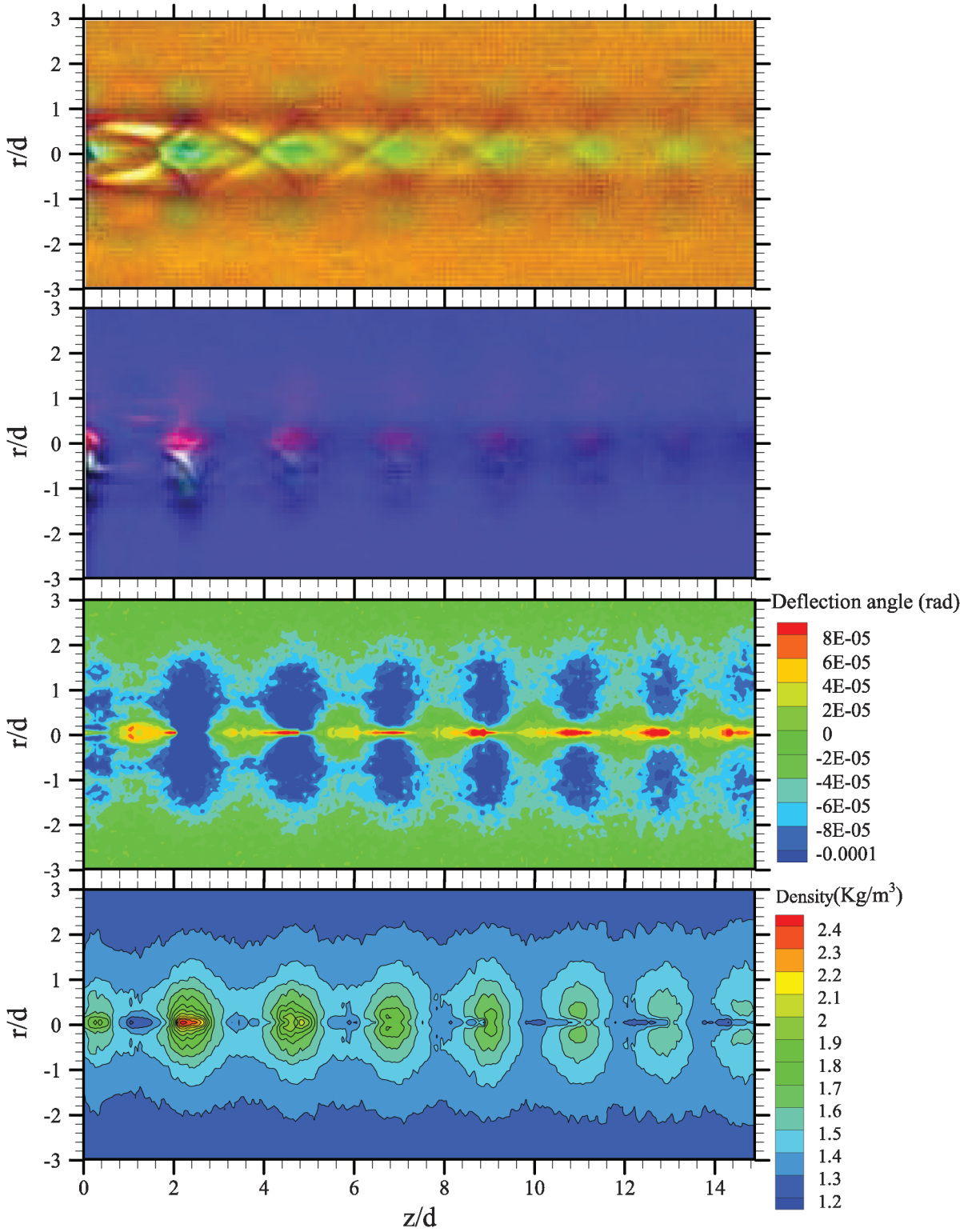

Fig. 5 Test results for $Ps = 860$ kPa showing a) rainbow schlieren image using a symmetric filter, b) rainbow schlieren image using an asymmetric filter, c) contour plot of deflection angle, and d) contour plot of density field.

unity (i.e., $Me \leq 1.0$), the density increase signifies subsonic compression at the orifice exit. Subsequently, the subsonic flow accelerates to reach supersonic conditions by $z/d = 1.0$ or upstream of the normal shock located at $z/d = 1.6$. Figure 7d shows the axial profile of the normalized Mach number, although the crossover point from subsonic to supersonic flow cannot be ascertained because the exit Mach number is not precisely known. Unlike the sonic nozzle, which results in uniform choked flow at the exit ($Me = 1$), the Mach number at the orifice exit is determined by the flow field generated within the orifice as conceptualized in Fig. 8 [29]. Evidently, the flow becomes supersonic downstream of the vena contracta formed within the orifice. The supersonic flow is reflected from the orifice channel wall, which results in subsonic flow across the normal shock in the center region and supersonic flow downstream of the reflected shock in the annulus region. Thus, the orifice exit flow consists of a subsonic slip strip with nearly sonic velocity surrounded by the supersonic flow in the annulus. Results in Fig. 7 are consistent with this explanation, although the exact details require direct measurements within the orifice that are difficult if not impossible to obtain. The normalized Mach number profile in Fig. 7d indicates the

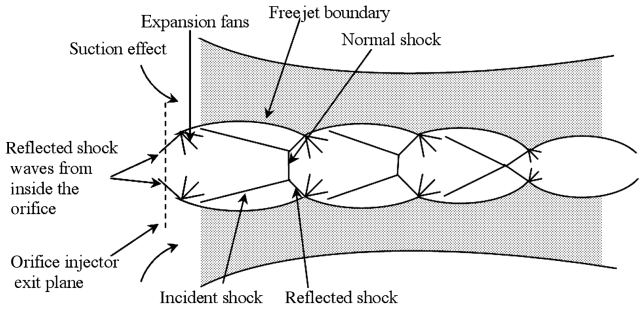

Fig. 6 Illustration of the shock-cell structures downstream of the orifice injector.

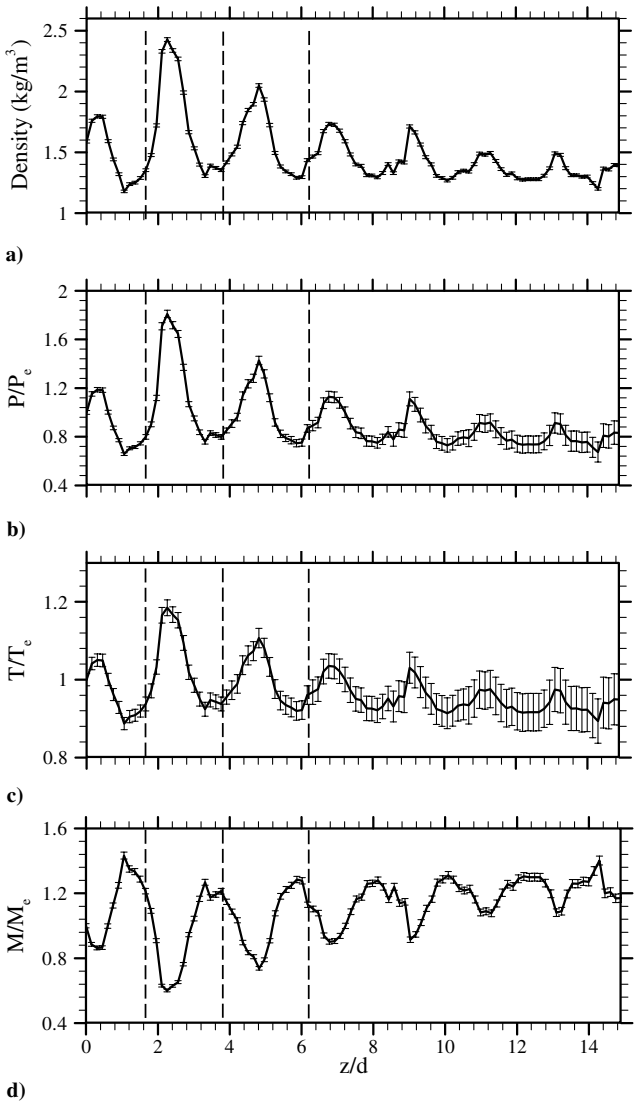

Fig. 7 Jet centerline profiles for $Ps = 860$ kPa a) density, b) normalized static pressure, c) normalized static temperature, and d) normalized Mach number.

Mach disk at the centerline is present only in the first 2–3 shock-cell structures, which is also supported by the schlieren visualization of Fig. 5a. At subsequent locations, the normalized Mach number exceeds 1.0, which suggests intersecting incident shock waves resulting in supersonic flow at the jet center.

Figure 9 shows the radial density profiles at various axial locations upstream (Fig. 9a) and around (Fig. 9b) the first normal shock. In a sonic nozzle, the density profile at the exit will be uniform, which is not the case in the present study as shown by the profile at $z/d = 0.1$

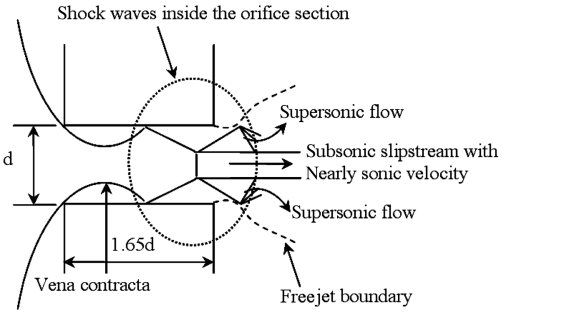

Fig. 8 Illustration of the shock-cell structures inside the orifice injector.

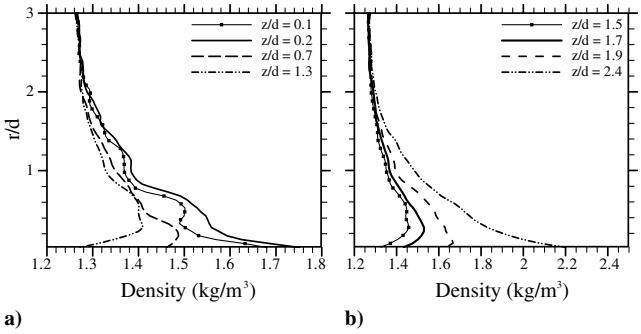

Fig. 9 Radial profiles of density for $Ps = 860$ kPa a) near the injector exit, and b) across and downstream of the normal shock.

(in Fig. 9a) with steep radial density gradients. The density is highest at the center ($r/d = 0.0$) and it decreases in the radial direction until about $r/d = 0.5$ or the orifice tip. This result supports the preceding explanation, suggesting that the orifice exit flow is subsonic (but nearly sonic) in the center region and supersonic in the outer annulus region. Beyond the orifice tip or between $r/d = 0.5$ and 0.7, the density increases slightly because of the weak compression wave, a result consistent with the illustration in Fig. 8. In the shear layer outside the supersonic freejet boundary (or $r/d > 0.7$), the density change is attributed to the flow entrainment processes. The subsonic shear layer extends up to about $r/d = 2.0$, where the density reaches the ambient value. Increase in density at the downstream location of $z/d = 0.2$ suggests that the flow within the freejet boundary ($r/d = 0.7$) decelerates between $z/d = 0.1$ and 0.2. The deceleration period is brief because by $z/d = 0.7$ the density has decreased significantly, indicating rapid flow acceleration. The decrease in density is highest at the center, where the flow is accelerating from subsonic to supersonic conditions. This trend continues between $z/d = 0.7$ and 1.3, with much of the density change occurring in the core region within $r/d < 0.5$. Profiles in Fig. 9b depict an increase in density between $z/d = 1.5$ and 1.6 caused by the compression across the normal shock in the center region and the reflected shock in the outer region. Interestingly, the density increase continues farther downstream of the normal and reflected shock waves, evidently because of the change in the flow cross-sectional area.

Figure 10 presents the details of the cyclic structures in the shear layer outside the freejet. The density at all radial locations in the shear layer varies in a cyclic manner. The oscillation period of the flow in the shear layer and that within the freejet is the same, indicating that the two regions are coupled. The density oscillation amplitude is higher at radial locations closer to the freejet and it decreases as the ambient conditions are reached at $r/d = 2.0$.

Finally, profiles in Fig. 11 illustrate the effects of the supply pressure on the jet flow structure. At a supply pressure of 720 kPa, the density profile along the centerline is similar to that at the higher pressure of 860 kPa (i.e., the density increases slightly at the orifice exit and subsequently varies in a cyclic manner, with mean and amplitude decreasing in the streamwise direction). The normalized Mach number profiles also indicate trends similar to those at the

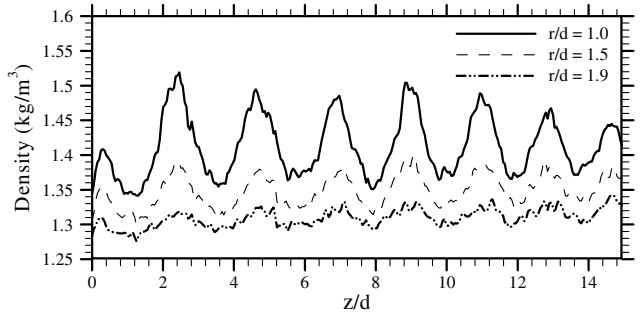

Fig. 10 Axial profiles of density outside the supersonic freejet boundary for *Ps* = 860 kPa.

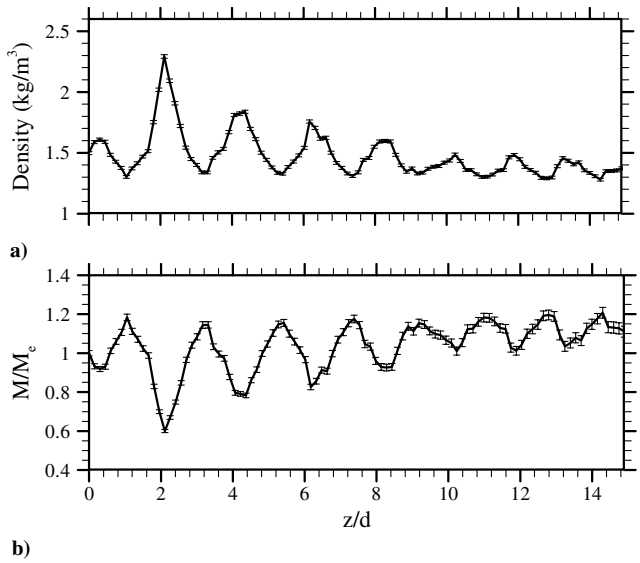

Fig. 11 Profiles at the jet centerline for *Ps* = 720 kPa a) density, and b) normalized Mach number.

higher supply pressure. The normal shock is likely present in the initial 2–3 shock-cell structures, whereas supersonic flow marked by the intersecting incident shock waves occurs in the downstream structures. At an even lower supply pressure of 515 kPa, Fig. 12 shows that density rise at the orifice exit is much greater. The corresponding normalized Mach number profile suggests that the flow at the centerline is subsonic in the first few shock-cell structures, and it becomes supersonic farther downstream, where the incident shock waves intersect with each other at the jet center. Again, this result can be explained in the context of the shock-cell structure formed inside the orifice (see Fig. 8), which leads to subsonic flow at

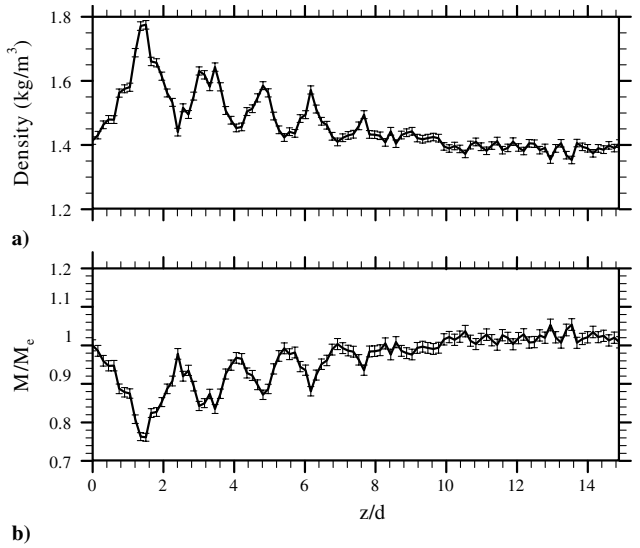

Fig. 12 Profiles at the jet centerline for *Ps* = 515 kPa a) density, and b) normalized Mach number.

the jet core and supersonic flow in the annular region. Figure 13 shows the density contour plot for supply pressure of 525 kPa. Figure 13 shows that the cyclic increase and decrease in density at various radial locations around the jet center leads to shock-cell structures located approximately at $z/d = 0.8$ to 2.4 and $z/d = 2.4$ to 4.0. This result can be related to the shock structure formed within the orifice as illustrated in Fig. 8. Evidently, the shock structure in the jet flow is the continuation of that initiated inside the orifice, an observation also made from Figs. 5d, 7a, and 9 for the higher supply pressure of 860 kPa. Accordingly, the orifice exit flow is highly nonuniform because the flow is subsonic flow in the center region and supersonic in the annular region.

VI. Conclusions

We have applied the miniature-RSD technique to measure density in supersonic microjets exhibiting complex interactions among shock waves. Spatial resolution of 25 μm was achieved in an axisymmetric volume of 1.5 mm radius and 7.5 mm length. These high-resolution measurements helped in explaining the flow field of an underexpanded microjet from an orifice, relevant to leakage from compressed gas storage facilities. Structurally, the flow field of the microjet is similar to its macrojet counterpart. The flow at the orifice exit was subsonic in the center region and supersonic in the outer annulus region, unlike the uniform sonic flow achieved with a contoured nozzle. For the first few shock-cell structures, the jet flow at the centerline undergoes compression across the normal shock, as

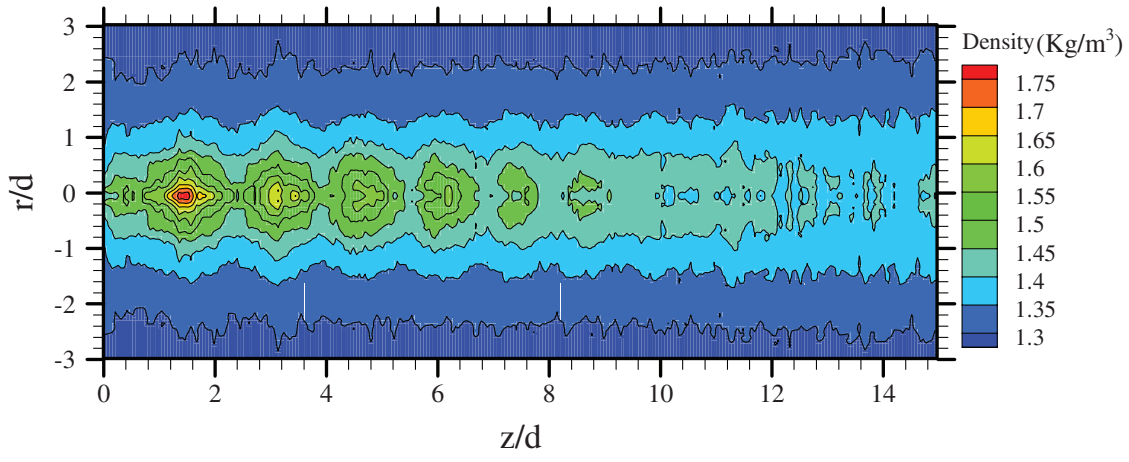

Fig. 13 Contour plot of the density field for *Ps* = 515 kPa.

well as in the supersonic region upstream and subsonic region downstream of the normal shock. The structure of the shock-cells was affected by the supply pressure. Given the high uncertainty of intrusive probe measurements in shock-cell structures and difficulty of obtaining high-resolution full field data, the mRSD technique appears to be a very promising approach for scalar measurements in supersonic flows. The study demonstrates the vast potential of the schlieren technique for quantitative scalar measurements when it is combined with advanced optical hardware, modern image processing, and computerized tomography. For example, the mRSD apparatus can be integrated with a high-speed imaging system to acquire time-resolved measurements or acoustic signatures in unsteady flows. In general, the mRSD technique is applicable for scalar measurements in macroscale supersonic jets, although the present implementation was limited to the steady, axisymmetric underexpanded microjets with a maximum jet exit Mach number of 1.6. For 3-D flows, the Abel inversion procedure must be replaced with a tomographic algorithm using multiple direction measurements. Based on the uncertainty propagation analysis, the maximum uncertainty in density measurements is within 1% of the reading. The density measured by the mRSD technique can be accurately related to other scalar properties (e.g., pressure, temperature, Mach number) using mass and momentum conservation equations (viz., Rankine–Hugoniot relations across the shock), although the isentropic relationships used in the present study introduced errors that accumulated with the downstream direction as the flow passed through more shock.

Acknowledgments

This work was supported in part by the Physical Sciences Division of NASA's Office of Biological and Physical research under grant NNC04GA22G and by the Combustion Research Facility at Sandia National Laboratories.

References

[1] Avduevsky, V. S., Ashratov, E. A., Ivanov, A. V., and Pirumov, U. G., *Gas Dynamics of Supersonic Nonisobaric Jets*, Mashinostroenie, Moscow, 1989, p. 320 (in Russian).

[2] Cheng, L. S., and Lee, K. S., "Numerical Simulations of Underexpanded Supersonic Jet and Free Shear Layer Using WENO Schemes," *International Journal of Heat and Fluid Flow*, Vol. 26, No. 5, 2005, pp. 755–770. doi:10.1016/j.ijheatfluidflow.2005.01.006

[3] Dillmann, A., Wetzel, T., and Soeller, C., "Interferometric Measurement and Tomography of the Density Field of Supersonic Jets," *Experiments in Fluids*, Vol. 25, Nos. 5–6, 1998, pp. 375–387. doi:10.1007/s003480050244

[4] Faris, G. W., and Byer, R. L., "Three-Dimensional Beam-Deflection Optical Tomography of a Supersonic Jet," *Applied Optics*, Vol. 27, No. 24, 1988, pp. 5202–5212.

[5] Lee, M. P., McMillin, B. K., and Hanson, R. K., "Temperature Measurements in Gases by Use of Planar Laser-Induced Fluorescence Imaging of NO," *Applied Optics*, Vol. 32, No. 27, 1993, pp. 5379–5396.

[6] Naik, S. V., Kulatilaka, W. T., and Lucht, R. P., "Development of High-Spectral-Resolution Planar Laser-Induced Fluorescence Imaging Diagnostics for High-Speed Gas Flow," AIAA Paper 2008-0246, 2008.

[7] Woodmansee, M. A., Lucht, R. P., and Dutton, J. C., "Development of High-Resolution N2 Coherent Anti-Stokes Raman Scattering for Measuring Pressure, Temperature, and Density in High-Speed Gas Flows," *Applied Optics*, Vol. 39, No. 33, 2000, pp. 6243–6256. doi:10.1364/AO.39.006243

[8] Panda, J., and Seasholtz, R. G., "Velocity and Temperature Measurement in Supersonic Free Jets Using Spectrally Resolved Rayleigh Scattering," AIAA Paper 1999-0296, 1999.

[9] Panda, J., and Seasholtz, R. G., "Measurement of Shock Structure and Shock-Vortex Interaction in Underexpanded Jets Using Rayleigh Scattering," *The Physics of Fluids*, Vol. 11, No. 12, 1999, pp. 3761–3777. doi:10.1063/1.870247

[10] Gad-el-Hak, M., "The Fluid Mechanics of Microdevices—The Freeman Scholar Lecture," *Journal of Fluids Engineering*, Vol. 121, No. 1, 1999, pp. 5–33. doi:10.1115/1.2822013

[11] Gravesen, P., Branebjerg, J., and Jensen, O. S., "Microfluidics—A Review," *Journal of Micromechanics and Microengineering: Structures, Devices, and Systems*, Vol. 3, No. 4, 1993, pp. 168–182. doi:10.1088/0960-1317/3/4/002

[12] Alvi, F. S., Elavarasan, R., Shih, C., and Garg, G., "Active Control of Supersonic Impinging Jets Using Microjets," *AIAA Fluids 2000 Conference*, AIAA Paper 2000-2236, June 2000.

[13] Santiago, J. G., Wereley, S. T., Meinhart, C. D., Beebe, D. J., and Adrian, R. J., "A Micro Particle Image Velocimetry System," *Experiments in Fluids*, Vol. 25, No. 4, 1998, pp. 316–319. doi:10.1007/s003480050235

[14] Meinhart, C. D., and Zhang, H., "The Flow Structure Inside a Microfabricated Inkjet Printhead," *Journal of Microelectromechanical Systems*, Vol. 9, No. 1, 2000, pp. 67–75. doi:10.1109/84.825779

[15] Synnergren, P., Larsson, L., and Lundstrom, T. S., "Digital Speckle Photography: Visualization of Mesoflow Through Clustered Fiber Networks," *Applied Optics*, Vol. 41, No. 7, 2002, pp. 1368–1373. doi:10.1364/AO.41.001368

[16] Buttner, L., Czarske, J., and Knuppertz, H., "Laser-Doppler Velocity Profile Sensor with Submicrometer Spatial Resolution that Employs Fiber Optics and a Diffractive Lens," *Applied Optics*, Vol. 44, No. 12, 2005, pp. 2274–2280. doi:10.1364/AO.44.002274

[17] Onofri, F., "Three Interfering Beams in Laser Doppler Velocimetry for Particle Position and Microflow Velocity Profile Measurements," *Applied Optics*, Vol. 45, No. 14, 2006, pp. 3317–3324. doi:10.1364/AO.45.003317

[18] Scroggs, S. D., and Settles, G. S., "An Experimental Study of Supersonic Microjets," *Experiments in Fluids*, Vol. 21, No. 6, 1996, pp. 401–409. doi:10.1007/BF00189042

[19] Phalnikar, K. A., Alvi, F. S., and Shih, C., "Behavior of Free and Supersonic Impinging Microjets," AIAA Paper 2001-3047, 2001.

[20] Phalnikar, K. A., Kumar, R., and Alvi, F. S., "Experiments on Free and Impinging Supersonic Microjets," *Experiments in Fluids*, Vol. 44, No. 5, 2008, pp. 819–830. doi:10.1007/s00348-007-0438-4

[21] Satti, R. P., Kolhe, P. S., Olcmen, S., and Agrawal, A. K., "A Miniature Rainbow Schlieren Deflectometry System for Quantitative Measurements in Micro Jets and Flames," *Applied Optics*, Vol. 46, No. 15, 2007, pp. 2954–2962. doi:10.1364/AO.46.002954

[22] Greenberg, P. S., Klimek, R. B., and Buchele, D. R., "Quantitative Rainbow Schlieren Deflectometry," *Applied Optics*, Vol. 34, No. 19, 1995, pp. 3810–3822.

[23] Al-Ammar, K., Agrawal, A. K., Gollahalli, S. R., and Griffin, D., "Application of Rainbow Schlieren Deflectometry for Concentration Measurements in an Axisymmetric Helium Jet," *Experiments in Fluids*, Vol. 25, No. 2, 1998, pp. 89–98. doi:10.1007/s003480050211

[24] Pasumarthi, K. S., and Agrawal, A. K., "Schlieren Measurements and Analysis of Concentration Field in Self-Excited Helium Jets," *Physics of Fluids*, Vol. 15, No. 12, 2003, pp. 3683–3692. doi:10.1063/1.1623490

[25] Wong, T., and Agrawal, A. K., "Quantitative Measurements in an Unsteady Flame Using High-Speed Rainbow Schlieren Deflectometry," *Measurement Science and Technology*, Vol. 17, No. 6, 2006, pp. 1503–1510. doi:10.1088/0957-0233/17/6/031

[26] Agrawal, A. K., Albers, B. W., and Griffin, D. W., "Abel Inversion of Deflectometric Measurements in Dynamic Flows," *Applied Optics*, Vol. 38, No. 15, 1999, pp. 3394–3398. doi:10.1364/AO.38.003394

[27] Anderson, J. D., *Modern Compressible Flow: With Historical Perspective*, 3rd ed., McGraw–Hill, New York, 2003, Chap. 3.

[28] Coleman, H. W., and Steele, W. G., Jr., *Experimentation and Uncertainty Analysis for Engineers*, 2nd ed., Wiley, New York, 1999, Chap. 3.

[29] Ward–Smith, A. J., "Critical Flowmetering: The Characteristics of Cylindrical Nozzles with Sharp Upstream Edges," *International Journal of Heat and Fluid Flow*, Vol. 1, No. 3, 1979, pp. 123–132. doi:10.1016/0142-727X(79)90028-6

A. Naguib
Associate Editor